Available online at www.sciencedirect.com
ScienceDirect
International Journal of Thermal Sciences 48 (2009) 985–997
International Journal of Thermal Sciences
www.elsevier.com/locate/ijts

Jet impingement onto a conical cavity: Effects of annular nozzle outer angle and jet velocity on heat transfer and skin friction

S.Z. Shuja, B.S. Yilbas *, S. Khan

ME Department, KFUPM, Dhahran 31261, Saudi Arabia

Received 29 April 2007; received in revised form 16 July 2008; accepted 16 July 2008

Available online 8 August 2008

Abstract

Jet impingement onto a conical cavity results in complicated flow structure in the region of the cavity. Depending on the nozzle geometric configurations and jet velocities, enhancement in the heat transfer rates from the cavity surface is possible. In the present study, annular nozzle and jet impingement onto a conical cavity are considered and heat transfer rates from the cavity surfaces are examined for various jet velocities, two outer angles of the annular nozzle, and two cavity depths. A numerical scheme adopting the control volume approach is used to simulate the flow situation and predict the heat transfer rates. It is found that increasing jet velocity at the nozzle exit modifies the flow structure in the cavity while altering the heat transfer rates and skin friction; in which case, increasing nozzle outer angle and jet velocity enhances the heat transfer rates and skin friction.

Keywords: Annular nozzle; Conical cavity; Jet impingement; Heat transfer; Skin friction

1. Introduction

Gas assisted processing is commonly used in laser machining applications. In this case, assisting gas emerging from the nozzle impinges onto the irradiated region. Since the laser irradiated region is at elevated temperature, the flow structure developed within the irradiated region influences the heat transfer rates and skin friction in this region. However, laser beam irradiation results in cavity formation at the solid surface. The cavity is at elevated temperature while impinging assisting gas jet is at room temperature. This situation influences the end product quality through modifying the heat transfer rates from the irradiated surface. Since the flow structure in the irradiated region depends on the jet velocity and geometric configuration of the nozzle used, investigation into the flow structure due to various jet velocities at the nozzle exit and nozzle angles becomes necessary.

Considerable research studies were carried out to examine jet impingement and heat transfer rates from the impingement surface. Confined impinging and opposing jets are studied by Hosseinalipour and Mujumdar [1]. They indicated that the predictions of impinging jets agree with the experimental results when the turbulence model was selected properly. Jet impingement and heat transfer were considered by Herwig et al. [2]. They indicated that the instability created in the jet through the vortex shedding improved the heat transfer as compared to a steady impinging jet. Seyed-Yagoobi [3] studied the heat transfer characteristics of the jet impingement emanating from different types of nozzles. He indicated that self-oscillating jet impinging nozzle provided improved heat transfer performance when the nozzle-to-plate spacing was less than the optimal spacing for the plain jet emerging from the nozzle. Amano and Brandt [4] investigated the flow structure due to jet impingement onto a flat plate and flowing into an axisymmetric cavity. They showed that the near-wall models for the kinetic energy and turbulent shear stress gave good predictions of the skin friction coefficients. The effects of nozzle diameter on heat transfer and flow structure due to impinging jet were examined by Lee and Lee [5]. They showed that the local Nusselt number increased with increasing nozzle diameter in the stagnation region while keeping the other flow parameters constant, which was attributed to an increase in the jet momentum and turbulence in-

* Corresponding author.
E-mail address: bsyilbas@kfupm.edu.sa (B.S. Yilbas).

1290-0729/$ – see front matter
doi:10.1016/j.ijthermalsci.2008.07.005

Nomenclature

H	enthalpy
h	heat transfer coefficient
K	thermal conductivity
k	turbulent kinetic energy
p	pressure
P	rate of production
R_{ij}	Reynolds stress
R_{ih}	energy generation due to Reynolds stress
Re	Reynolds no.
r	distance in the radial direction
t	time
T	temperature
u^*	friction velocity
U	arbitrary velocity
V	axial velocity component
$\forall$	volume
x	distance in the axial direction

Greek

α	thermal diffusivity
Γ	arbitrary diffusion coefficient
ε	energy dissipation
λ	turbulence intensity
μ	dynamic viscosity
ν	kinematic viscosity
ρ	density (function of temperature and pressure for gas)
τ	shear stress
σ	variable Prandtl no.
θ	nozzle cone angle
Φ	viscous dissipation
ϕ	arbitrary variable
Π	energy transport due to pressure excluding strain interactions
Π^w	energy transport due to wall reflection
Λ	energy transport by diffusion

Subscript

amb	ambient
gas	fluid (gas) side
i, j	arbitrary direction
jet	gas jet at inlet
l	laminar
m	mean
max	maximum
p	a typical node in the computational grid
ref	reference
t	turbulent
solid	solid side
v	viscous sublayer
w	wall

tensity level with the large nozzle diameter. Heat transfer due to jet impingement onto a flat plate and influence of nozzle-plate spacing on the heat transfer rates were examined by Lytle and Webb [6]. They indicated that the accelerating fluid between the nozzle and the plate gap as well as an increase in the local turbulence resulted in substantially increase in the local heat transfer rates from the plate surface. The jet impingement and heat transfer from a small heat source was studied by Womac et al. [7]. They showed that under the free-surface jet conditions, the heat transfer coefficient could be attenuated by bulk warming of the thin fluid sheet flowing over the surface, provided that the nozzle diameter was small and the flow velocity was low. Large diameter jet impingement onto the surfaces was examined by Zhang and Ibrahim [8]. They tested various turbulence models and indicated that k–ω turbulence model was sensitive to the inlet boundary conditions despite the fact that k–ω model predictions agreed well with the experimental data. Jet impingement from off-axial nozzle for laser processing was investigated by Ilavarasan and Molian [9]. They indicated that the principle of the off-axial gas jet was to provide straight non-turbulent flow to the laser processing section. The dynamic characteristics of gas flow inside a laser cut kerf were examined by Man et al. [10]. They indicated that the behavior of the jet was strongly influenced by the stand-off distance and the thickness of the workpiece. Convective heat and mass transfer due to jet impingement on a moving surface was examined by Zumbrunnen [11]. He used the similarity solution to the momentum equations to obtain the flow structure in the stagnation region. Shuja et al. [12] investigated previously jet impingement and the heat transfer from the impingement surface. However, in the simulations, the effect of jet velocity at nozzle exit on the heat transfer rates and skin friction was omitted due to simplicity. Consequently, extension of the previous study becomes necessary to include the effects of jet velocity on the heat transfer rates and the skin friction.

In the present study, jet impingement onto a conical cavity with elevated wall temperature is considered and the effects of jet velocity on the heat transfer rates and the skin friction are examined. In the simulations, four jet velocities, two annular nozzle outer cone angles and two conical cavity depths are accommodated. The selection of the magnitude of the jet velocity is due to the jet velocities used in the laser gas assisted processing. The Reynolds stress turbulence model is used to account for the turbulence while air is employed as working fluid.

2. Mathematical modeling

The steady flow conditions with the compressibility and variable properties of the working fluid are considered to formulate the jet impingement onto the cylindrical cavity. A constant temperature is considered at the cavity wall to resemble the laser produced cavity, i.e. cavity wall temperature is kept at 1500 K as similar to the melting temperature of the substrate

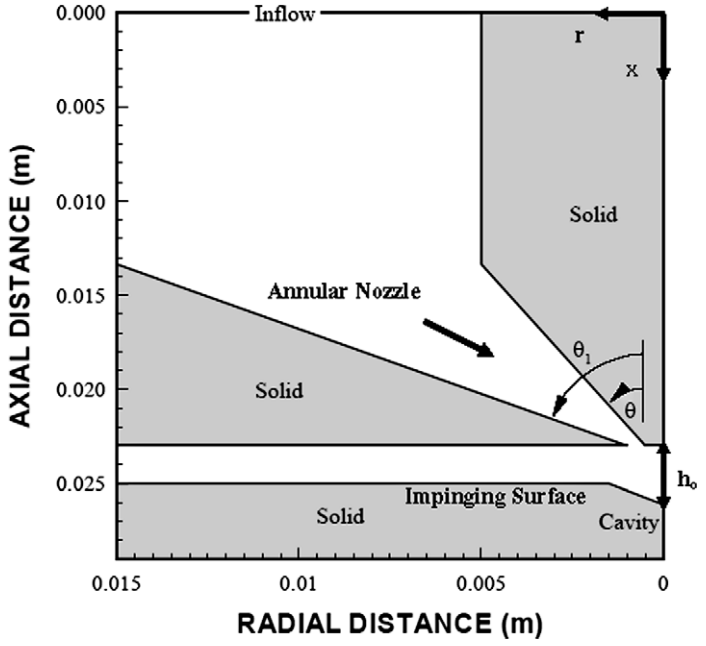

(a)

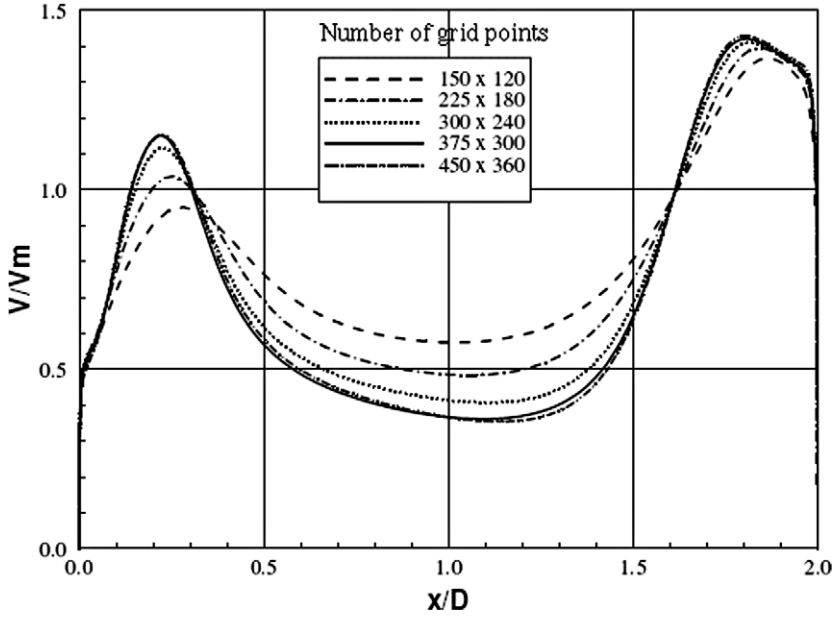

(b)

Fig. 1. (a) Geometric view of the annular nozzle and the cavity. θ represents the annular nozzle cone angle. $\mathbf{h_o}$ represents the stand off distance. (b) Grid independent test results obtained for dimensionless velocity magnitude along the symmetry axis. D is the hydraulic diameter of the annular nozzle exit and V_m is the mean velocity at the nozzle exit ($V_m = V_{\text{jet}}$ at the nozzle exit). It should be noted that x-axis location $x/D = 2$ corresponds to 0.023 m from the x-axis origin.

Table 1
Size and depth of the cavity, and annular nozzle outer cone angle

Cavity diameter (m)	Cavity depth (m)	Annular nozzle angles	
		Inner angle (θ°)	Outer angle ($\theta_1{}^\circ$)
0.003	0.0005	25	55
0.003	0.001	40	70

material. The geometric arrangements of the annular nozzle and the cavity are shown in Fig. 1(a), while the nozzle and the cavity configurations are given in Table 1.

2.1. Flow equations

The governing flow and energy equations for the axisymmetric impinging steady jet can be written in the Cartesian tensor notation as:

(i) The continuity equation

$$\frac{\partial}{\partial x_i}(\rho U_i) = 0 \tag{1}$$

(ii) The momentum equation

$$\frac{\partial}{\partial x_i}(\rho U_i U_j) = \frac{\partial p}{\partial x_j} + \frac{\partial}{\partial x_i}\left[\mu\left(\frac{\partial U_i}{\partial x_j} + \frac{\partial U_j}{\partial x_i}\right) - \rho R_{ij}\right] \tag{2}$$

(iii) The energy equation

$$\frac{\partial}{\partial x_i}(\rho U_i H) = \frac{\partial}{\partial x_i}\left[\frac{\mu}{\sigma}\frac{\partial H}{\partial x_i} - \rho R_{ih}\right] \tag{3}$$

The flow field is turbulent; therefore, Reynolds stress turbulence model (RSM), which is based on the second-moment closure, is used in the analysis. The selection of the turbulence model is based on the previous study [13]; in which case, standard two equation models over estimates the turbulent kinetic energy generation in the stagnation region [14]. The transport equation of the Reynolds stress (R_{ij}) is

$$\frac{\partial}{\partial x_m}(U_m R_{ij}) = P_{ij} + \Lambda_{ij} - \varepsilon_{ij} + \Pi_{ij} + \Pi_{ij}^{w} \tag{4}$$

where $P, \Lambda, \varepsilon, \Pi$ and Π^w are the rate of production, transport by diffusion, rate of dissipation, transport due to turbulent pressure excluding strain interactions and transport due to wall reflection, respectively. Eq. (4) consists of six partial differential equations; one for the transport of each of the six independent Reynolds stresses. The production term (P_{ij}), diffusion (Λ_{ij}), dissipation (ε_{ij}), transport due to turbulent pressure (Π_{ij}) and the modeling of the wall reflection (Π_{ij}^{w}) are referred to [15].

2.2. Flow boundary conditions

Four boundary conditions are considered in accordance with the geometric arrangement of the problem, as shown in Fig. 1(a).

2.2.1. Solid wall

For the solid wall, the no-slip condition is assumed at the solid wall, and the boundary condition for the velocity at the solid wall therefore is

$$U_i = 0 \tag{5}$$

2.2.2. Generalized wall functions for normal and shear turbulent stresses for the RSM model

When the flow is very near the wall, it undergoes a rapid change in direction; therefore, the wall-functions approach is not successful in reproducing the details of the flow. Consequently the turbulent stresses and fluxes at the near-wall grid points are calculated directly from their transport equations. In this case, the near-wall region lying between the wall and the near-wall computational node at x_p can be represented by two layers: the fully viscous sublayer, defined by $Re_v = x_v\sqrt{k_v}/\nu \approx 20$, and a fully-turbulent layer. The wall shear stress near the wall is employed, i.e. $\overline{vw}|_{z_v} = \tau_w/\rho$, which serves as the boundary condition for the $\overline{vw}$ transport equation.

In relation to normal stresses, the turbulence energy must decrease quadratically towards a value of zero at the wall; therefore, a zero-gradient condition for the normal stresses is physically realistic. This situation is insufficient to ensure an accurate numerical representation of near-wall effects. An improved approach for internal cells is needed in respect of evaluating volume integrated production and dissipation of normal stresses (these are normally evaluated at cell centers, using linear interpolation, and then multiplied by the cell volume). Considering $\overline{v}^2$ as an example, the volume-integrated production of $\overline{v}^2$ between the wall and the P-node may be approximated by,

$$\int_{\Delta r}\int_{0}^{z_p} P_{22}\, d\forall \cong \int_{\Delta r}\int_{x_v}^{x_p} -2\overline{vw}\frac{\partial V}{\partial x}\, d\forall = 2\tau_w\left(\frac{V_p - V_v}{x_p - x_v}\right)x_p \Delta r \tag{6}$$

where V_p and V_v follow from the log-law. No contribution arises from the viscous sublayer, since $\overline{vw} = 0$ in this layer. An analogous integration of the dissipation rate with the assumptions,

$$\varepsilon = \frac{2\nu k_v}{x_v^2}, \qquad 0 \leqslant x \leqslant x_v$$

$$\varepsilon = \frac{C_\mu^{3/4} k_p^{3/2}}{\kappa x_v}, \qquad x_v \leqslant x \leqslant x_p$$

leads to

$$\int_{\Delta r}\int_{0}^{x_p} \varepsilon\, d\forall \cong \left[\frac{2\nu k_p}{x_v} + \frac{C_\mu^{3/4} k_p^{3/2}}{\kappa}\ln\left(\frac{x_p}{x_v}\right)\right]\Delta r \tag{7}$$

an analogous treatment is applied to $\overline{v}^2$, while the production of $\overline{w}^2$ in the viscous and turbulent near wall layers region is zero.

The values resulting from Eqs. (6) and (7) are added, respectively, to the volume-integrated generation and dissipation computed for the upper half of the near-wall volume. It should be noted that for the wall-law approach, the near-wall dissipation (ε_p) is not determined from its differential equation applied to the near-wall cell surrounding the node. Instead, and in accordance with the log law, this value is obtained via the length scale from $\varepsilon_p = C_\mu^{3/4} k_p^{3/2}/\kappa z_p$, which serves as the boundary conditions for inner cells.

Table 2
Mean jet velocity at the nozzle exit

Mean jet velocity, V_{jet} (m/s)
25
50
75
100

2.2.3. Inlet conditions

The boundary conditions for temperature and the mean jet velocity at the nozzle exit is introduced. Therefore, at the nozzle exit: T = specified (300 K) and the values of the mean jet velocity is given in Table 2. The selection of the values of the mean velocities is due to the gas jet velocities, in general, used in laser gas assisted processing.

The values of ♣ and ε are not known at the inlet, but can be determined from the turbulent kinetic energy, i.e.

$$k = \lambda \bar{u}^2 \tag{8}$$

where $\bar{u}$ is the average inlet velocity and λ is a percentage.

The dissipation is calculated from $\varepsilon = C_\mu k^{3/2}/aD$, where D is the diameter. The values $\lambda = 0.03$ and $a = 0.005$ are commonly used and may vary slightly in the literature [16].

2.2.4. Outlet

The flow is considered to be extended over a long domain; therefore, the boundary condition (outflow boundaries, Fig. 1(a)) for any variable ϕ is

$$\frac{\partial \phi}{\partial x_i} = 0 \tag{9}$$

where • is the normal direction at outlet.

2.2.5. Symmetry axis

At the symmetry axis, the radial derivative of the variables is set to zero, i.e.

$$\frac{\partial \phi}{\partial r} = 0 \tag{10}$$

except for

$$V = \overline{vw} = \overline{vh} = \overline{wh} = 0 \tag{11}$$

2.3. Solid side

2.3.1. Constant wall temperature boundary

Two constant temperature boundaries are considered. The first one is in the radial direction far away from the symmetry axis at a constant temperature $T = T_{\text{amb}}$ (300 K). It should be noted that the constant temperature boundary condition is set at different locations in the radial directions. The boundary condition ($T =$ constant) located in the radial direction had no significant effect on the temperature and flow field in the stagnation region. Therefore, this boundary condition is set for a radial distance of 0.015 m from the symmetry axis. The second constant temperature boundary is set at the cavity walls (as shown in Fig. 1(a)) at $T =$ constant (1500 K).

2.3.2. Solid fluid interface

The coupling of conduction within the solid and convection within the fluid, termed conjugation, is required for the present analysis at the solid fluid interface. The appropriate boundary conditions are continuity of heat flux and temperature and are termed boundary conditions of the fourth kind, i.e.

$$T_{w_{\text{solid}}} = T_{w_{\text{gas}}} \quad \text{and} \quad K_{w_{\text{solid}}} \frac{\partial T_{w_{\text{solid}}}}{\partial x} = K_{w_{\text{gas}}} \frac{\partial T_{w_{\text{gas}}}}{\partial x} \tag{12}$$

No radiation loss from the solid surface is assumed due to the small surface area of the cavity.

The heat transfer coefficient is determined from:

$$h = \frac{(-k_{w_{\text{solid}}}(\frac{\partial T_{w_{\text{solid}}}}{\partial n}))}{(T_{w_{\text{gas}}} - T_{\text{ref}})} \tag{13}$$

Table 3
Air properties used in the simulation

Density	ρ (kg m^{-3})	Ideal gas ($\rho = P/R_{\mathbf{A}\oplus}$)
Thermal conductivity	K (W m^{-1} K^{-1})	0.0242
Specific heat capacity	c_p (J kg^{-1} K^{-1})	1006.43
Viscosity	ν (kg m^{-1} s^{-1})	1.7894×10^{-5}

where $(\partial T_{w_{\text{solid}}}/\partial n)$ is the temperature gradient in the solid normal to the cavity surface while T_{ref} is the reference temperature and equals to the jet temperature at the nozzle exit. It should be noted that at the gas temperature in the vicinity of the wall ($T_{w_{\text{gas}}}$) is considered when computing the heat transfer coefficient.

The wall shear stress is determined from the rate of fluid strain at the cavity wall, which is:

$$\tau = \mu\left(\frac{\partial V}{\partial n}\right) \tag{14}$$

where $(\partial V/\partial n)$is the rate of fluid strain at the cavity wall and n represents the direction normal to the cavity surface.

2.4. Gas properties

The equation of state is used for air and the properties employed are given in Table 3.

3. Numerical method and simulation

A control volume approach is employed to discretize the governing equations. The discretization procedure is given in the literature [17]. The problem of determining the pressure and satisfying continuity may be overcome by adjusting the pressure field so as to satisfy continuity. A staggered grid arrangement is used in which the velocities are stored at a location midway between the grid points, i.e. on the control volume faces. All other variables including pressure are calculated at the grid points. This arrangement gives a convenient way of handling the pressure linkages through the continuity equation and is known as Semi-Implicit Method for Pressure-Linked Equations (SIMPLE) algorithm. The details of this algorithm are given in the literature [17].

The computer program used for the present simulation can handle a non-uniform grid spacing. In each direction fine grid spacing near the gas jet impinging point and the cavity is allocated while gradually increased spacing for locations away from the cavity is considered. Elsewhere the grid spacing is adjusted to maintain a constant ratio of any of two adjacent spacing. The number of grid planes used normal to the x and r directions are 375 and 300, respectively, in the simulations. The grid independence tests were conducted and it is observed that the grid selected results in the grid-independent solution. Fig. 1(b) shows the grid independent test results.

Nine variables are computed at all grid points; these are: two velocity components, local pressure, five turbulence quantities and the temperature.

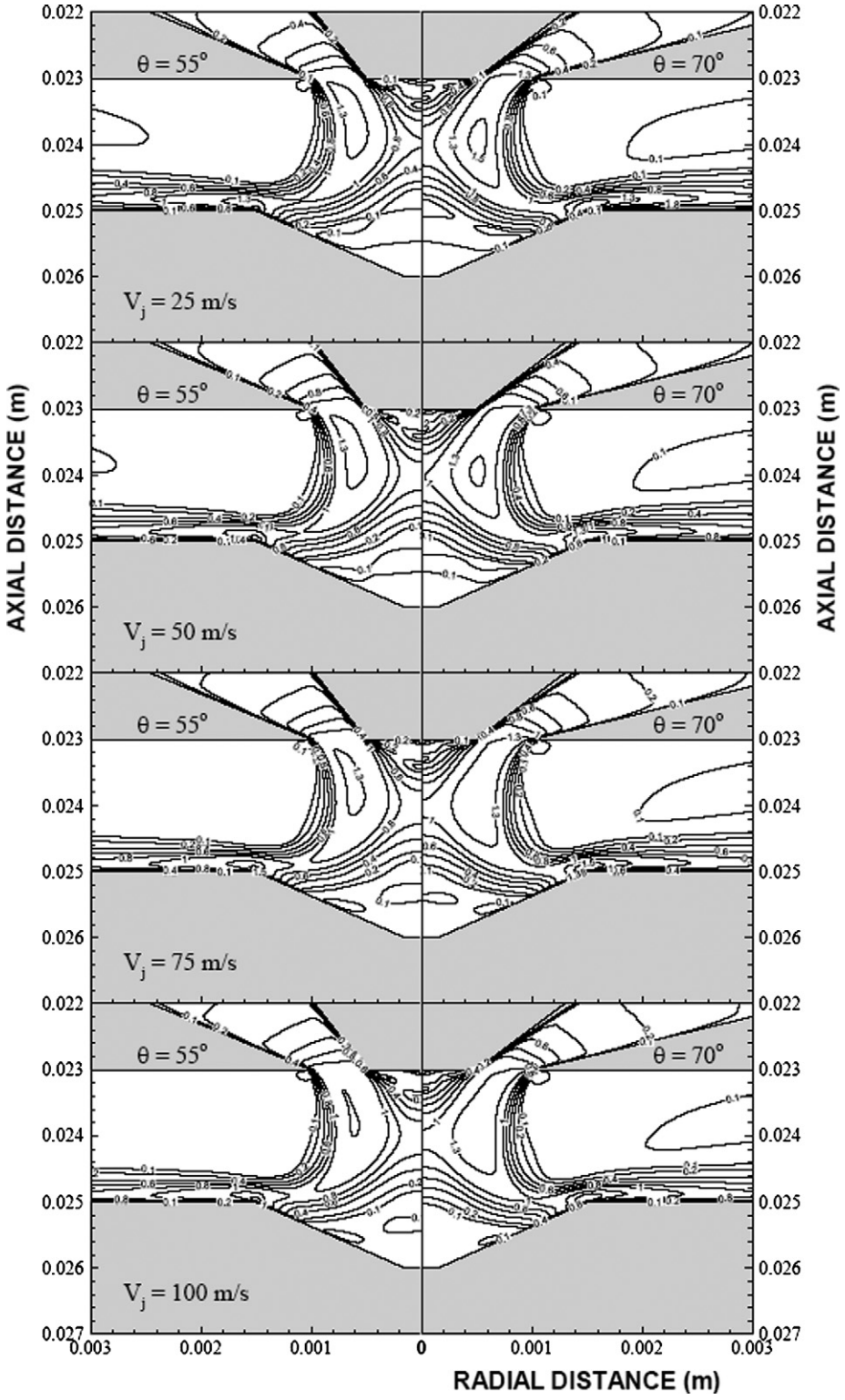

Fig. 2. Normalized velocity magnitude (V/V_{jet}) for the conical cavity depth of 1 mm.

4. Results and discussion

Jet impingement onto a conical cavity is considered and the effects of annular nozzle exit velocity and nozzle outer angle on the heat transfer rates and the skin friction are examined. Four jet velocities, two outer angles of annular nozzle, and two cavity depth are accommodated in the simulations. Air is considered as the working fluid.

Figs. 2 and 3 show contour plots of normalized velocity magnitude (V/V_{jet}) in the cavity region for different jet velocities at the nozzle exit, two depths of the conical cavity and two outer cone angles of the annular nozzle. Jet impingement results in a

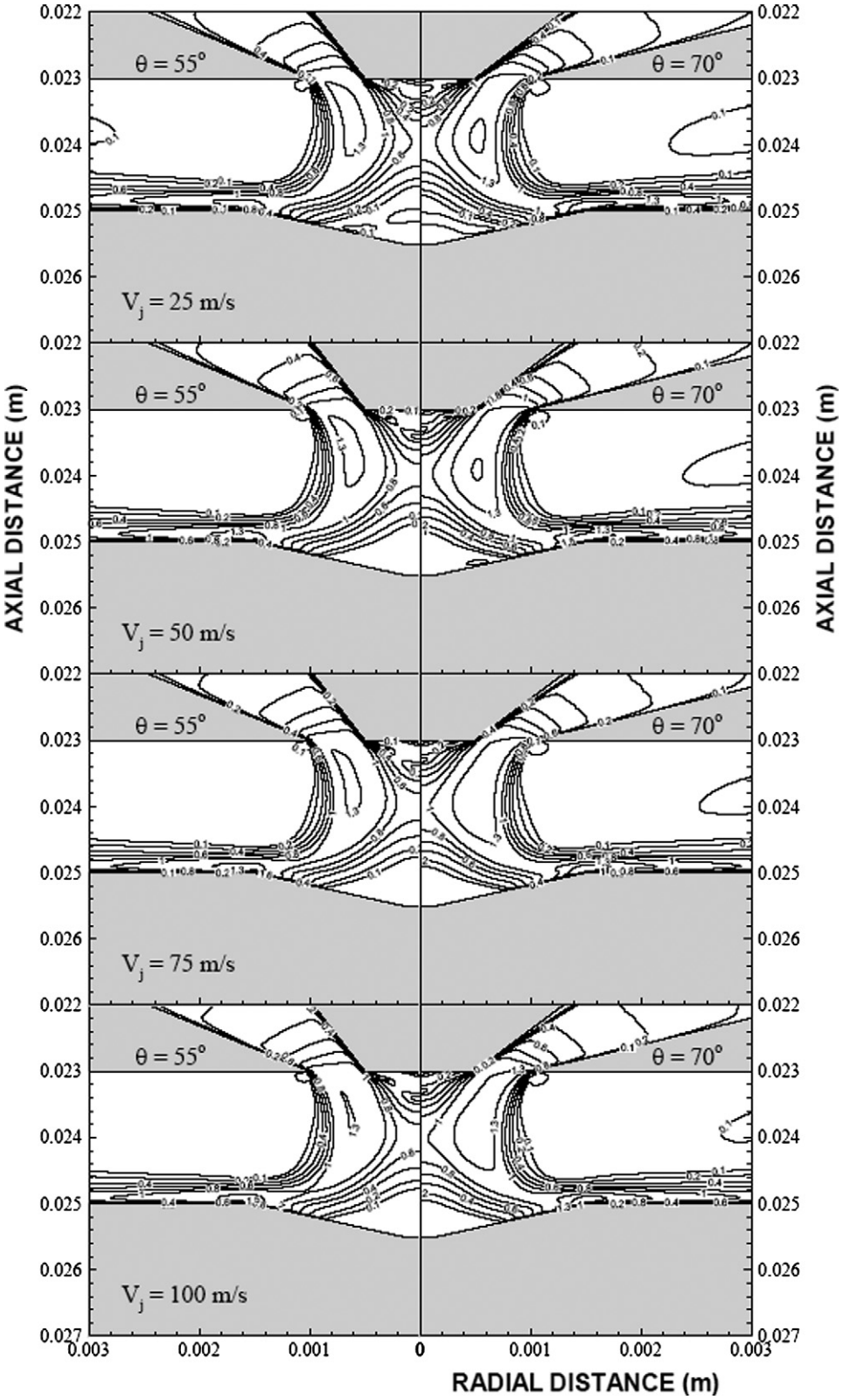

Fig. 3. Normalized velocity magnitude (V/V_{jet}) for the conical cavity depth of 0.5 mm.

stagnation zone along the symmetry axis in the cavity. The impinging jet under goes a streamline curvature above the cavity inlet. This is particularly true for outer cone angle of 55°. Moreover, the radial expansion of the jet is observed for outer angle of 70°; in which case, normalized velocity (V/V_{jet}) becomes 1.3 indicating the radial expansion of the jet in the nozzle exit region. Increasing average jet velocity at the nozzle exit suppresses this situation due to enhancement of axial momentum

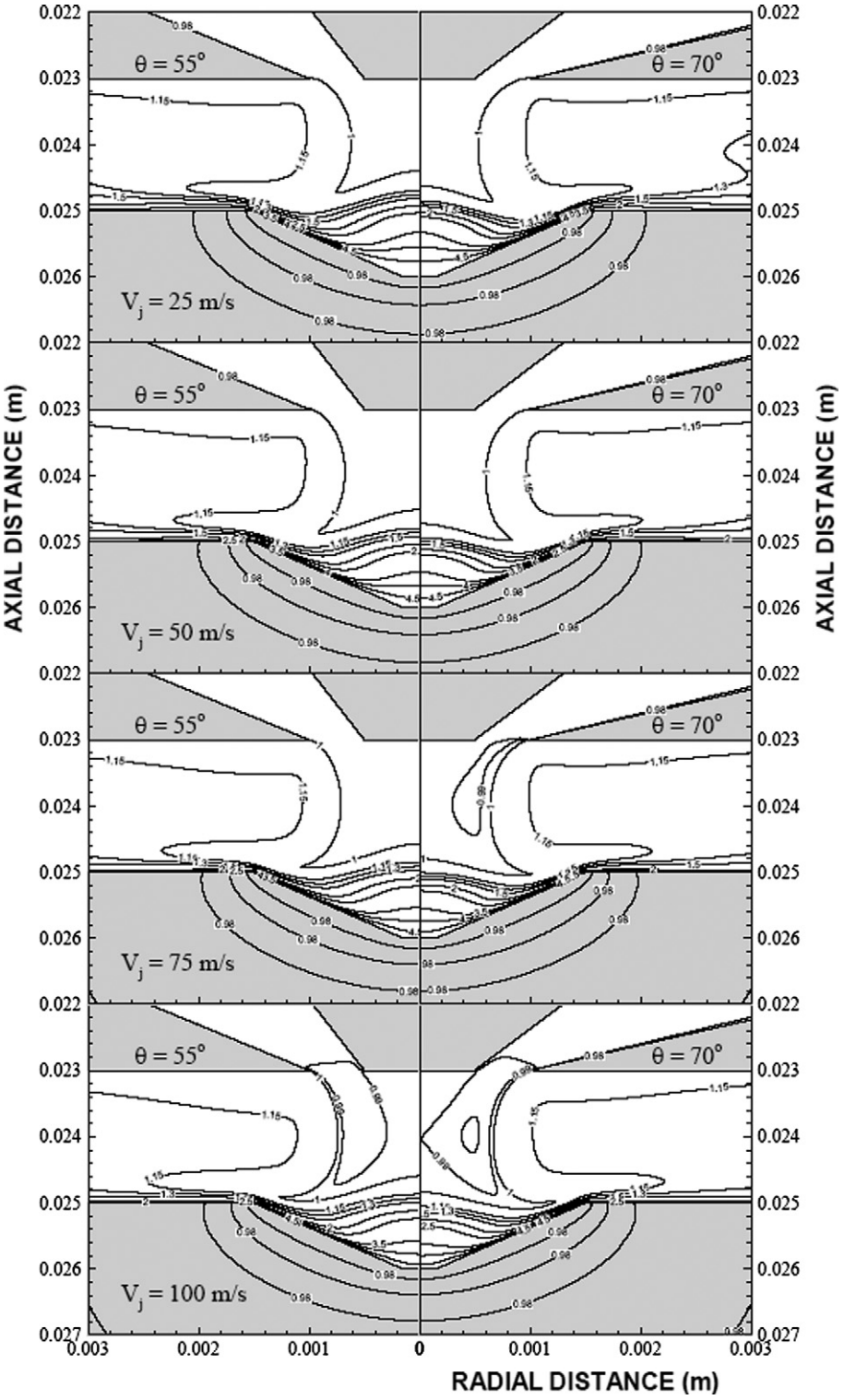

Fig. 4. Normalized temperature (T/T_{jet}) for the conical cavity depth of 1 mm.

along the symmetry axis. Radial acceleration of the flow in the cavity, due to pressure differential, mixes with the radially expanding jet in the region next to the cavity exit. This situation is more pronounced for the outer cone angle of 70°. In the case of a deep cavity (cavity depth = 1 mm), stagnation zone moves further into the cavity around the symmetry axis. Although, the radial flow developed in the cavity accelerates further towards the cavity exit because of the high pressure differential accruing in the region next to the stagnation zone, the impinging jet emerging from the nozzle suppresses the flow acceleration towards the cavity exit. This is more pronounced for the outer cone angle of 55°. Consequently, the axial momentum of the impinging jet influences the flow acceleration in the region of the cavity exit. The accelerated flow expands semi-radially at

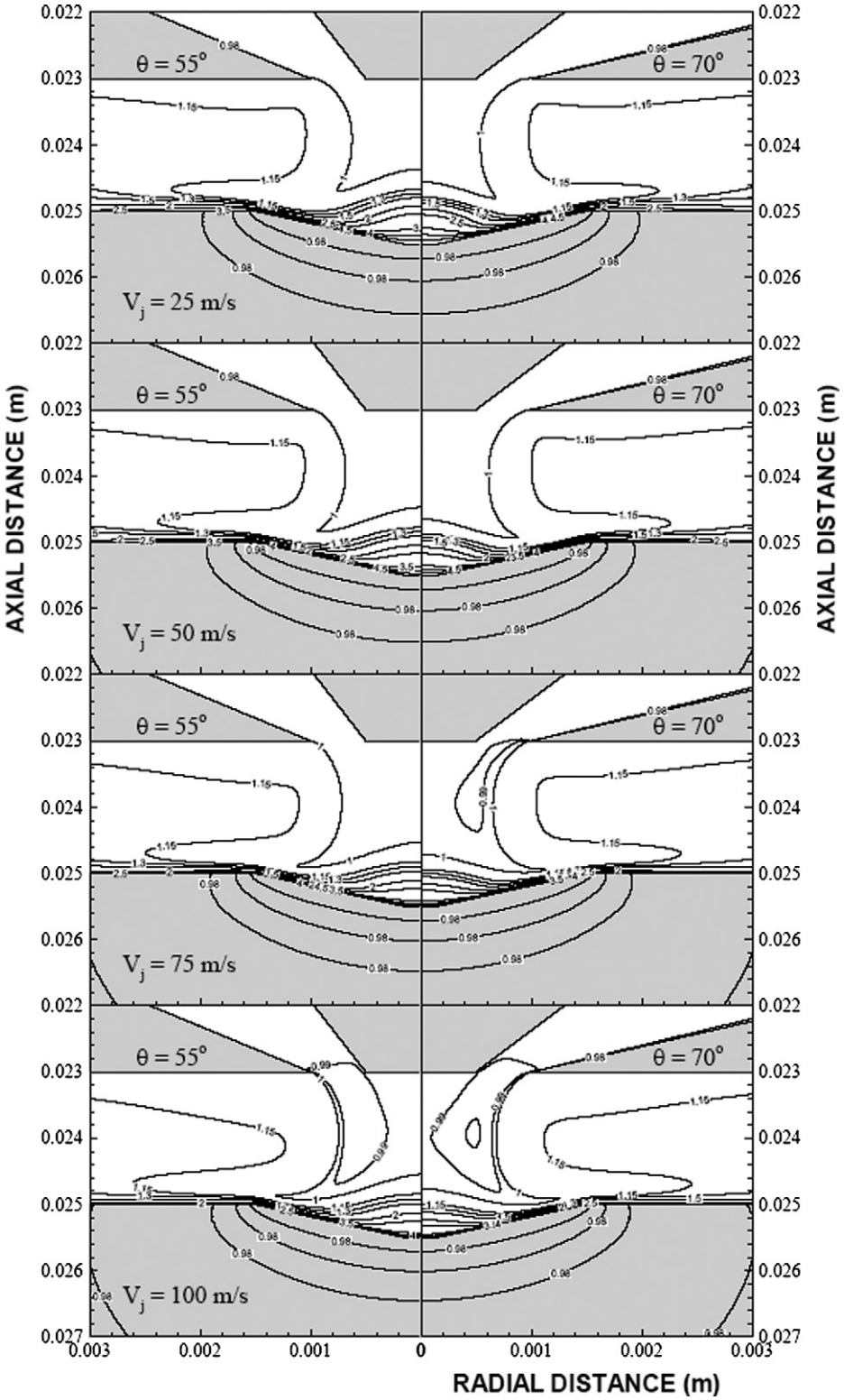

Fig. 5. Normalized temperature (T/T_{jet}) for the conical cavity depth of 0.5 mm.

the cavity exit for the outer cone angle of 70°. Consequently, the flow structure generated in the cavity changes with the annular nozzle outer cone angle. As the average jet velocity at the nozzle exit increases, the semi-radial expansion of the flow is partially suppressed because of the axial momentum of the impinging jet.

Normalized temperature (T/T_{jet}) contours in the cavity region corresponding to different average jet velocities at the nozzle exit, two cavity depths, and two annular nozzle outer cone angles are shown in Figs. 4 and 5. Temperature contours follow almost the velocity contours in and above the cavity. Due to high temperature at the cavity wall, the flow in the cavity is

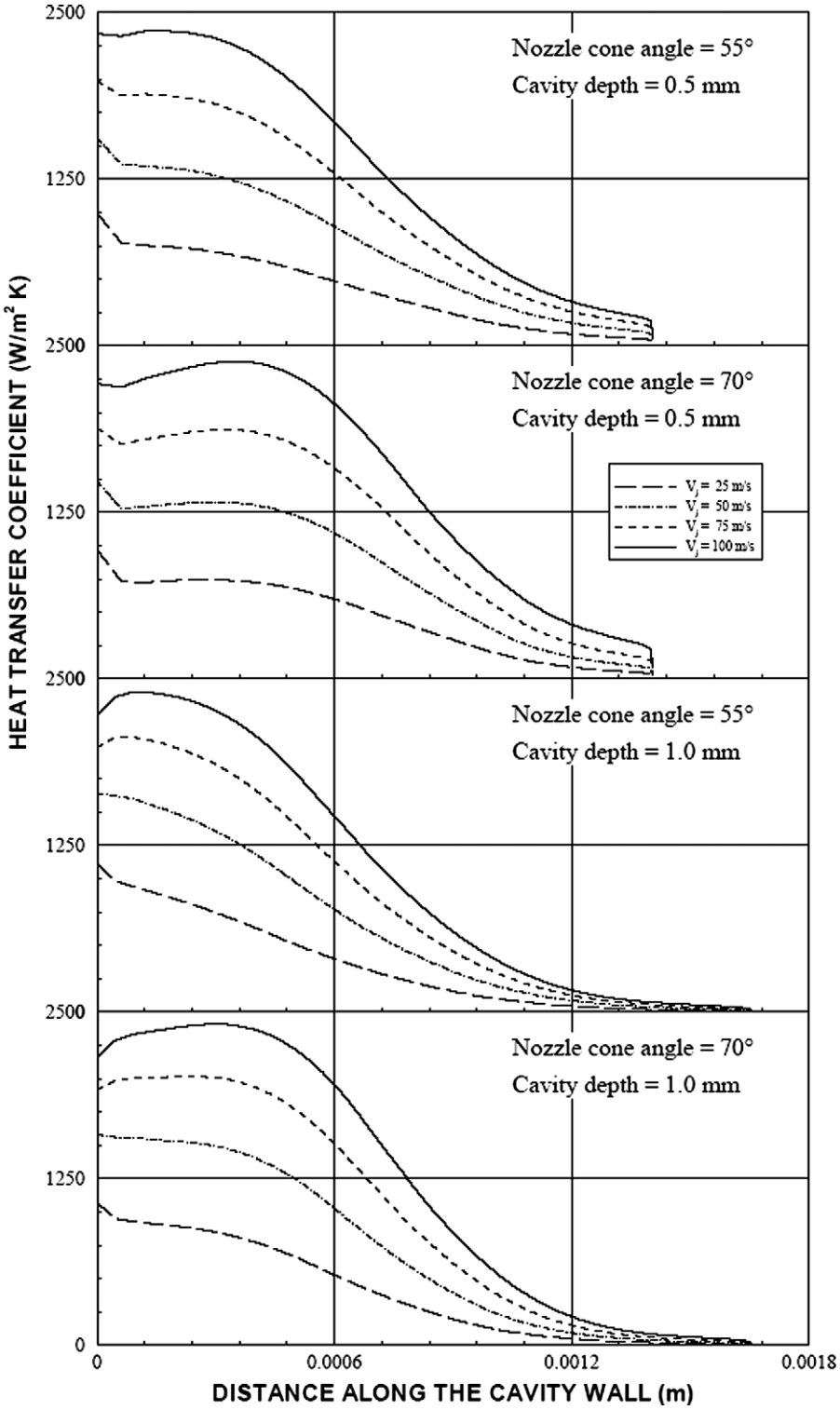

Fig. 6. Heat Transfer coefficient for the conical cavity wall surface. The location 0 along the cavity wall surface represents the cavity edge.

at higher temperature than that of in the impinging jet. This situation is more pronounced for the outer cone angle of 55°. The flow developed in the cavity suffers from the conduction and the convection heating due to the low velocity. Consequently, conduction heating in the fluid enhances temperature rise in the flow. This results in thickening of the thermal boundary layer in the cavity. As the average jet velocity at nozzle exit increases, thermal boundary layer thickness reduces in the cavity and the radial acceleration of the flow due to the pressure differential suppresses further the thermal boundary layer thickness. Moreover, for the outer cone angle of 70°, the radial flow of the jet causes the flow mixing with the high temperature fluid emerging from the cavity in the region of the cavity exit. This results in extension of the high temperature region further towards the

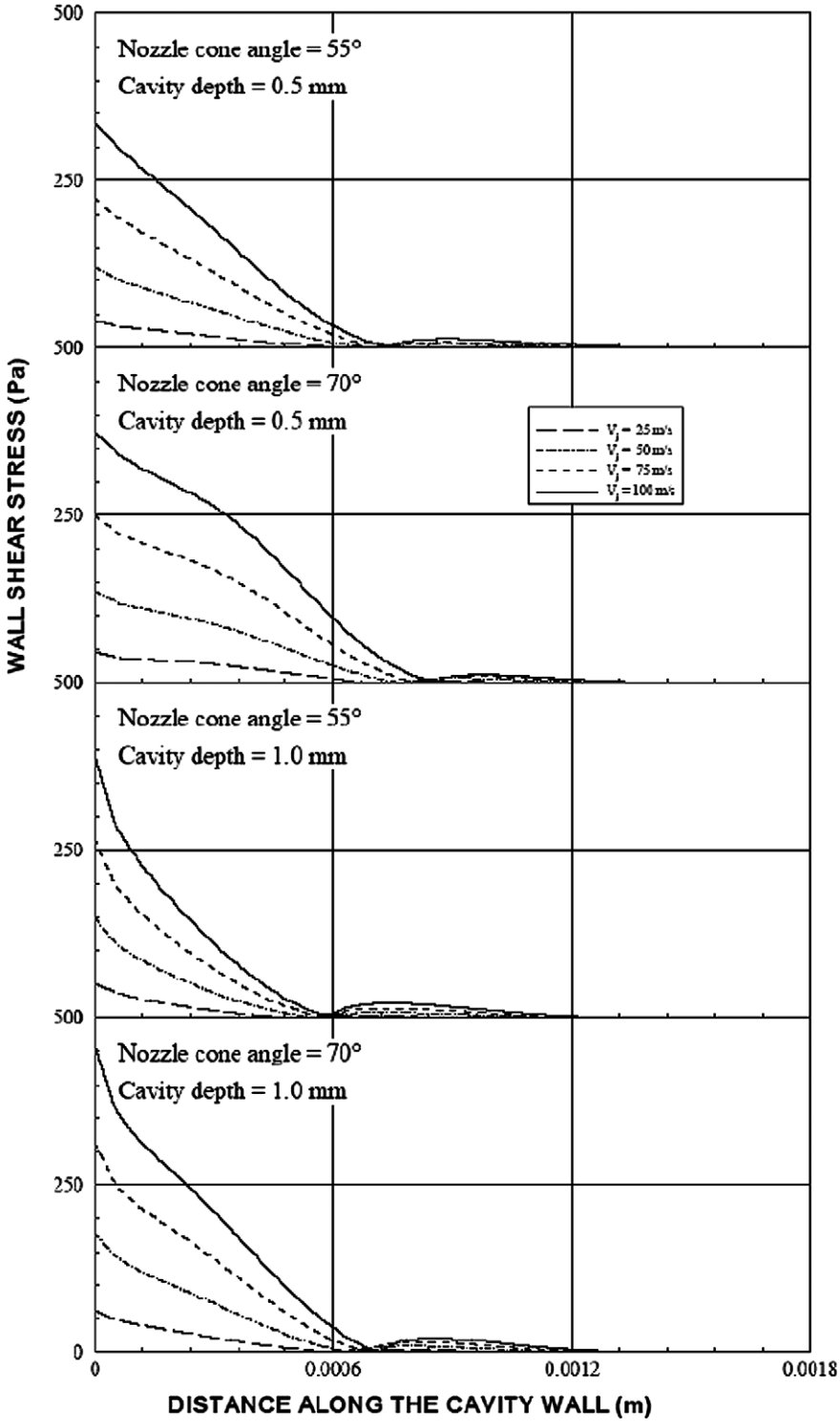

Fig. 7. Shear Stress at the conical cavity wall surface. The location 0 along the cavity wall surface represents the cavity edge.

downstream of the flow. This is also true for the outer cone angle of 55°, provided that this expansion is not as much extended as that of 70°. Consequently, annular nozzle cone angle and the average jet velocity at the nozzle exit have a coupling effect on the temperature behavior. In this case, increasing both the outer cone angle and the cavity depth enhances the extension of high temperature in the downstream stream of the flow field.

Fig. 6 shows heat transfer coefficient along the cavity wall for different average jet velocities at the nozzle exit, two cavity depths, and two cone angles of the annular nozzle. It should be noted that the distance in the figure represents the distance along cavity surface and the location 0 m along the cavity surface represents the cavity edge. Since the conical cavity is symmetrical, the heat transfer coefficient remains the same with the

rotation of the cavity surface along the symmetry axis. Therefore, the heat transfer coefficient is independent of the rotational angle along the symmetry axis. The heat transfer coefficient remains almost the same along the cavity surface in the region of the cavity exit and it decays sharply with increasing distance along the cavity surface against the symmetry axis (where $r = 0$ m). This is true for all the depths and the outer cone angles because of the flow mixing in the region of the cavity exit and the radial acceleration of the flow emanating from the cavity remains high in this region. Moreover, the sharp decay of the heat transfer coefficient is attributed to creeping like flow and the thick thermal boundary layer near to the stagnation zone; in which case, convection cooling of the cavity surface by the fluid is less as compared to the cavity exit region. Increasing average jet velocity at the nozzle exit enhances the heat transfer coefficient through increasing the convective heat transfer rates from the cavity surface. The flow acceleration in the radial direction in the cavity is responsible for the enhancement of heat transfer coefficient. Although impinging jet at high velocity moves the stagnation zone further inside the cavity, due to pressure differential in the region next to the stagnation zone, the radial acceleration enhances the flow velocity in the cavity. This reduces the thermal boundary layer thickness in the cavity and improves the heat transfer rates from the cavity surface. The radial acceleration of the flow, due to pressure differential in the cavity, also results in the maximum heat transfer coefficient moving in the cavity. This is true for all the cavity depths. Moreover, the location of the maximum heat transfer coefficient further moves into the cavity with increasing nozzle angle.

Fig. 7 shows the shear stress along the distance at the cavity wall for different average jet velocities at the annular nozzle exit, two cavity depths, and two annular nozzle outer cone angles. The wall shear stress attains maximum at the cavity exit and it decays sharply with increasing distance along the cavity surface against the symmetry axis. This situation is true for all the cavity depths and the outer cone angles of the nozzle. However, the gradual decay of the shear stress along the cavity surface occurs while reducing the jet velocity at the nozzle exit. This is because of the creeping like flow generated in the cavity. The rate of fluid strain remains low and the boundary layer thickness becomes thick in the cavity. This, in turn, results in low shear stress in the wall region of the cavity. Moreover, attainment of high values of the shear stress at the cavity exit is attributed to the radial flow in this region. In this case, the rate of fluid strain remains high and the boundary layer thickness becomes small. However, in the stagnation region, the flow velocity becomes small and the boundary layer thickness remains high; consequently, shear stress becomes small in the region close to the stagnation zone in the cavity. The shear stress attains slight high values for the outer cone angle of 70° and $V_{\text{jet}} = 100$ m/s. This is because of the radial acceleration of the flow in the region of the cavity wall generating the high shear stress in wall region of the cavity, particularly towards the cavity exit. In the case of deep cavity (cavity depth is 1 mm), similar situation is observed provided that the value of the shear stress increase slightly.

5. Conclusion

The flow emerging from the annular nozzle and impinging onto a conical cavity results in a stagnation zone along the symmetry axis in the cavity. The size of the stagnation zone is influenced by the annular nozzle outer cone angle, cavity depths, and the average jet velocity at the nozzle exit. In this case, increasing cavity depth (1 mm) and reducing both the outer cone angle (55°) and the average jet velocity at the nozzle exit enhances the size of the stagnation zone in the cavity. However, the radial expansion of the jet occurs for the annular nozzle outer cone angle of 70°. The radially accelerated flow emerging from the cavity mixes with the impinging jet in the region of the cavity exit. As the average jet velocity at nozzle exit increases, the flow mixing results in a complicated flow structure at the cavity exit, which modifies slightly the streamline curvature of the impinging jet. Moreover, the pressure differential in the cavity, in the neighborhood of the stagnation zone, is responsible for the radial acceleration of the flow in the cavity. This situation is more pronounced for the deep cavity and the nozzle outer cone angle of 70°. The heat transfer coefficient attains high values in the region of the cavity exit because of (i) the flow mixing in this region, and (ii) occurrence of the radially accelerated flow in this region. This is more pronounced for the high jet velocities at the nozzle exit. Moreover, the radial acceleration of the flow, due to pressure differential in the cavity, results in the maximum heat transfer coefficient occurring in the cavity and the location of the maximum heat transfer coefficient moves further into the cavity with increasing nozzle angle. The heat transfer coefficient reduces along the cavity surface against the symmetry axis. This is because of the thickening of the thermal boundary layer and low flow velocity, which suppresses the heat transfer rates from the cavity wall. The wall shear stress increases along the cavity surface towards the cavity exit. The attainment of high rate of fluid strain is responsible for the development of the high shear stresses. Moreover, the flow velocity remains low and the boundary layer thickness becomes large in the region close to the symmetry axis. This causes the low shear strain while lowering the shear stress in this region.

Acknowledgements

The authors acknowledge the support of King Fahd University of Petroleum and Minerals, Dhahran, Saudi Arabia, for this work.

References

[1] S.M. Hosseinalipour, A.S. Mujumdar, Comparative evaluation of different turbulence models for confined impinging and opposing jet flows, Numerical Heat Transfer, Part A (Applications) 28 (6) (1995) 647–666.
[2] H. Herwig, H. Mocikat, T. Gurtler, S. Goppert, Heat transfer due to unsteadily impinging jets, International Journal of Thermal Sciences 43 (8) (2004) 733–741.
[3] J. Seyed-Yagoobi, Enhancement of heat and mass transfer with innovative impinging jets, Drying Technology 14 (5) (1996) 1173–1196.
[4] R.S. Amano, H. Brandt, Numerical study of turbulent axisymmetric jets impinging on a flat plate and flowing into an axisymmetric cavity, Transactions of the ASME. Journal of Fluids Engineering 106 (4) (1984) 410–417.

[5] J. Lee, S. Lee, The effect of nozzle aspect ration on stagnation region heat transfer characteristics of elliptic impinging jet, International Journal of Heat and Mass Transfer 43 (2000) 555–575.
[6] D. Lytle, B.W. Webb, Air jet impingement heat transfer at low nozzle-plate spacings, International Journal of Heat and Mass Transfer 37 (12) (1994) 1687–1697.
[7] D.J. Womac, S. Ramadhyani, F.P. Incropera, Correlating equations for impingement cooling of small heat sources with single circular liquid jets, ASME Journal of Heat Transfer 115 (1993) 106–115.
[8] Z. Zhang, M. Ibrahim, CFD studies on a large diameter jet impingement flow, in: Proceedings of the ASME Heat Transfer/Fluids Engineering Summer Conference 2004, HT/FED 2004, 2004, pp. 185–192.
[9] P.M. Ilavarasan, P.A. Molian, Design, fabrication and testing of an off-axial gas jet nozzle for enhanced laser cutting, in: Proceedings of the Laser Materials Proceeding Conference, 1993, Laser Institute of America, 1994, pp. 350–360.
[10] H.C. Man, J. Duan, T.M. Yue, Design and characteristic analysis of supersonic nozzles for high gas pressure laser cutting, Journal of Materials Processing Technology 63 (1997) 217–222.
[11] D.A. Zumbrunnen, Convective heat and mass transfer in the stagnation region of a laminar planar jet impinging on a moving surface, Transactions of the ASME. Journal of Heat Transfer 113 (3) (1991) 563–570.
[12] S.Z. Shuja, B.S. Yilbas, M.O. Budair, Influence of conical and annular nozzle geometric configurations on flow and heat transfer characteristics due to flow impingement onto a flat plate, Numerical Heat Transfer, Part A 48 (2005) 917–939.
[13] S.Z. Shuja, B.S. Yilbas, M.O. Budair, Gas jet impingement on a surface having a limited constant heat flux area—various turbulence models, Numerical Heat Transfer, Part A 36 (2) (1999) 171–200.
[14] T.J. Craft, L.J.W. Graham, B.E. Launder, Impinging jet studies for turbulence model assessment. II. An examination of the performance of four turbulence models, Int. J. Heat Mass Transfer 36 (1993) 2685–2697.
[15] W.C. Lasher, D.B. Taulbee, Reynolds stress model assessment using round jet experimental data, International Journal of Heat and Fluid Flow 15 (5) (1994) 357–363.
[16] H.K. Versteeg, W. Malalasekera, An Introduction to Computational Fluid Dynamics, The Finite Volume Method, Longman Scientific and Technical, 1995.
[17] S.V. Patankar, Numerical Heat Transfer, McGraw-Hill, New York, 1980.